

# NiMn-based bimetal-organic framework nanosheets supported on multi-channel carbon fibers for efficient oxygen electrocatalysis

Cheng, Weiren; Lu, Xue Feng; Luan, Deyan; Lou, David Xiong Wen

2020

Cheng, W., Lu, X. F., Luan, D. & Lou, D. X. W. (2020). NiMn-based bimetal-organic framework nanosheets supported on multi-channel carbon fibers for efficient oxygen electrocatalysis. *Angewandte Chemie International Edition*, 59(41), 18234-18239.  
<https://dx.doi.org/10.1002/anie.202008129>

<https://hdl.handle.net/10356/147390>

<https://doi.org/10.1002/anie.202008129>

---

This is the peer reviewed version of the following article: Cheng, W., Lu, X. F., Luan, D. & Lou, D. X. W. (2020). NiMn-based bimetal-organic framework nanosheets supported on multi-channel carbon fibers for efficient oxygen electrocatalysis. *Angewandte Chemie International Edition*, 59(41), 18234-18239. <https://dx.doi.org/10.1002/anie.202008129>, which has been published in final form at <https://doi.org/10.1002/anie.202008129>. This article may be used for non-commercial purposes in accordance with Wiley Terms and Conditions for Use of Self-Archived Versions.

*Downloaded on 13 Mar 2024 15:22:53 SGT*

# NiMn-Based Bimetal-Organic Framework Nanosheets Supported on Multi-Channel Carbon Fibers for Efficient Oxygen Electrocatalysis

Weiren Cheng, Xue Feng Lu, Deyan Luan,<sup>\*</sup> and Xiong Wen (David) Lou<sup>\*</sup>

[\*] Dr. W. R. Cheng, Dr. X. F. Lu, Dr. D. Y. Luan, Prof. X. W. Lou

School of Chemical and Biomedical Engineering, Nanyang Technological University, 62 Nanyang Drive, Singapore 637459, Singapore

Email: dyluan@ntu.edu.sg; xwlou@ntu.edu.sg; davidlou88@gmail.com

Webpage: <http://www.ntu.edu.sg/home/xwlou/>

## Abstract

*Developing noble-metal-free bifunctional oxygen electrocatalysts is of great significance for several key energy conversion and storage systems, yet remains as a grand challenge. Herein, we have developed a transformation method for growing NiMn-based bimetal-organic framework (NiMn-MOF) nanosheets on multi-channel carbon fibers (MCCF) as a promising bifunctional oxygen electrocatalyst. Owing to the active NiMn-MOF nanosheets and their tight connection with the highly conductive MCCF support, the obtained MCCF/NiMn-MOFs manifest comparable electrocatalytic performance towards oxygen reduction reaction (ORR) with the commercial Pt/C electrocatalyst and superior performance towards oxygen evolution reaction (OER) to the benchmark RuO<sub>2</sub> electrocatalyst. X-ray absorption fine structure (XAFS) spectroscopy and density-functional theory (DFT) calculations reveal that the strong synergetic effect of adjacent Ni and Mn nodes within MCCF/NiMn-MOFs effectively promotes the thermodynamic formation of key \*O and \*OOH intermediates over active NiO<sub>6</sub> centers towards fast ORR and OER kinetics.*

**Keywords:** MOF; Multi-channel carbon fiber; ORR; OER; Electrocatalysis.

The electrochemical oxygen catalysis, including oxygen reduction reaction (ORR) and oxygen evolution reaction (OER), is of essential importance in modern high-energy-density systems including metal-air batteries, fuel cells, and electrolyzers.<sup>[1-5]</sup> To maximize the overall conversion efficiencies in these systems, it is urgently desired to develop highly efficient electrocatalysts to overcome the thermodynamically sluggish kinetics of oxygen electrocatalysis.<sup>[6-8]</sup> Up to now, the well-known oxygen electrocatalysts are mainly Pt- and/or Ru- based noble metals or metal oxides,<sup>[9-11]</sup> which yet greatly suffer from high cost and poor operation stability. Moreover, these Pt- or Ru-based catalysts are normally unable to simultaneously deliver high activity towards ORR and OER, which in turn would increase the processing cost and assembling complexity of the modern energy devices.<sup>[1,12]</sup> Therefore, it is a great challenge to seek efficient bifunctional oxygen electrocatalysts needed for the widespread deployment of these oxygen-involving technologies.

Metal-organic frameworks (MOFs), composed of organic ligands and well-dispersed metal nodes, have unique features of large specific surface areas, tunable pore sizes, adjustable chemical components, and surface functionality, which enables them as potentially promising noble-metal-free electrocatalysts.<sup>[7,13-16]</sup> Moreover, these MOFs with well-dispersed metal sites could offer ideal platforms for exploring the nature of active sites and the origin of electrocatalytic activity relative to conventional metal oxides and hydroxides.<sup>[14,17,18]</sup> Although tremendous efforts have been devoted, it is still difficult for the developed MOF-based electrocatalysts to perfectly balance the adsorption energetics of various oxo-intermediates towards highly efficient ORR and OER, owing to the insufficient understanding of the active sites and the underlying catalytic mechanism.<sup>[19,20]</sup> Additionally, the inaccessibility of internal metal nodes and intrinsically poor conductivity of bulk MOFs would also significantly undermine their electrocatalytic performance.<sup>[21-23]</sup> To overcome those issues, the introduction of synergistically bimetallic active sites in ultrathin MOFs combined with rational architectural design of carbon-matrix supports is anticipated to effectively lever the adsorption energetics of diverse oxo-intermediates, enlarge the numbers of surface active sites,

facilitate the charge transfer, and guarantee the stability of MOF-based electrocatalysts.<sup>[3,24-27]</sup> Furthermore, these hierarchical MOF nanosheets with full exposure of well-dispersed metal centers are very helpful for the atomic-level identification of real active sites and in-depth exploration of their electrocatalytic mechanisms.<sup>[14,28,29]</sup> Nevertheless, it remains a great challenge to directly integrate bimetallic MOF nanosheets onto conductive carbon-matrix supports.

Herein, we report a transformation method for growing hierarchical NiMn-MOF nanosheets on multi-channel carbon fibers (MCCF/NiMn-MOFs) involving a facile hydrothermal growth and subsequent ligand exchange. With the merits of the synergetic effect between Ni and Mn nodes in the MOF nanosheets, the as-obtained MCCF/NiMn-MOFs exhibit both high ORR and OER activities with a decent ORR onset potential of 0.85 V versus reversible hydrogen electrode (vs. RHE) and a superior OER overpotential of 280 mV at 10 mA cm<sup>-2</sup>, as well as robust stability in alkaline media. With a combination of synchrotron radiation X-ray absorption fine structure (XAFS) spectroscopy and density-functional theory (DFT) calculations, the atomic-level configurations of essentially active NiO<sub>6</sub> centers are identified and the intrinsic nature of bimetallic synergy of adjacent Ni and Mn nodes is clearly revealed in MCCF/NiMn-MOFs. More specifically, the strong coupling interactions of neighboring Ni and Mn nodes is helpful for the thermodynamic generation of key \*O and \*OOH intermediates during ORR and OER.

The MCCF/NiMn-MOFs are synthesized through a two-step method involving a hydrothermal synthesis and a subsequent ligand exchange procedure (see the Supporting Information (SI) for more details), as illustrated in **Figure 1**. More specifically, the interwoven MCCF with an average diameter of ~0.8 μm is employed as the conductive support (Figure S1 and S2, SI). Uniform NiMn layered double hydroxide (LDH) nanosheets are first grown on the surface of MCCF (MCCF/NiMn-LDH) by a facile hydrothermal process. Subsequently, these NiMn-LDH nanosheets are *in situ* transformed into NiMn-MOF nanosheets through a ligand exchange reaction. In this process, certain amounts of H<sup>+</sup> ions and naphthalenedicarboxyl groups are initially generated by the hydrolysis of 2,6-

naphthalenedicarboxyl acid ligands, and then the NiMn-LDH is locally dissolved accompanied by rapid nucleation of NiMn-MOF on the surface of MCCF, thanks to the etching of  $H^+$  and the chelation of naphthalenedicarboxyl groups.<sup>[30,31]</sup> Eventually, the NiMn-LDH nanosheets supported on MCCF are completely converted to NiMn-MOF nanosheets at the end of the ligand exchange reaction, thus forming the final MCCF/NiMn-MOFs. FESEM and TEM images (**Figure 2a-c**; Figure S3, SI) and XRD pattern (Figure S4a, SI) show that rigid NiMn-LDH nanosheets with a single-sheet thickness of ~50 nm densely stand over each MCCF after the hydrothermal synthesis.<sup>[32,33]</sup> Furthermore, the time-dependent FESEM images, XRD patterns and FTIR spectra (Figure S5, SI) suggest the complete transformation from NiMn-LDH to NiMn-MOFs after a 6-hour ligand exchange reaction, contributing to wrinkled NiMn-MOF nanosheets with a single-sheet thickness of ~40 nm fully supported on the surface of each MCCF (Figure 2d-f; Figure S6, SI).

The XRD pattern of MCCF/NiMn-MOFs (Figure S7a, SI) shows that the crystal structure of NiMn-MOF nanosheets is isostructural to that of the monoclinic Ni-based MOF (Cambridge Crystallographic Data Centre (CCDC) No. 985 792) and no diffraction peaks of metal hydroxide/oxide impurities are observed.<sup>[28,32,34]</sup> The high-angle annular dark-field scanning transmission electron microscopy (HAADF-STEM) image together with the energy-dispersive X-ray (EDX) spectroscopy elemental mapping images (Figure 2g; Figure S7b, SI) jointly show that NiMn-MOF nanosheets are densely and uniformly grown on each MCCF. Furthermore, the inductively coupled plasma-optical emission spectroscopy (ICP-OES) result shows the atomic ratio of Ni:Mn in MCCF/NiMn-MOFs is about 0.17:1, which is close to the EDX result (~0.19:1; Figure S7b, SI). The specific surface area of MCCF/NiMn-MOFs is as high as 100.3 m<sup>2</sup> g<sup>-1</sup> (Figure S8, SI). Those morphological and structural characterizations confirm the successful synthesis of hierarchical NiMn-MOF nanosheets supported over MCCF.

To provide in-depth insights into the atomic and electronic structure of MCCF/NiMn-MOFs, synchrotron radiation XAFS measurements were carried out. The  $k^3\chi(k)$  oscillation curves of Mn and

Ni *K*-edge (**Figure 3a**; Figure S9, SI) appear very similar in shape and oscillating frequency over the whole range of 2.1-11.4 Å<sup>-1</sup>, suggesting similar site occupancies of Ni and Mn nodes in both NiMn-MOFs and Ni-MOFs.<sup>[35-37]</sup> Furthermore, as seen from the Fourier transform curves of the extended XAFS (EXAFS) for Ni and Mn *K*-edge in Figure 3b, the dominant peak located at ~1.57 Å is well assigned to the nearest coordination shell of the metal-oxygen bonds (M-O, M = Ni, Mn), and the relatively weak peaks at ~2.82 and 3.30 Å are associated with the higher coordination shell contributions of M-C/O and M-M/M-O bonds, respectively.<sup>[14,38,39]</sup> It is noteworthy that the nearest M-O peak of Mn *K*-edge shifts towards high *R* direction by about 0.07 Å relative to that of Ni *K*-edge, indicating longer Mn-O bonds for Mn nodes. The EXAFS fitting results (Figure S10 and Table S1, SI) suggest that the coordination number of M-O bonds is quantitatively determined to be ~6 for both Ni and Mn nodes, contributing to octahedral configurations of NiO<sub>6</sub> and MnO<sub>6</sub> centers in MCCF/NiMn-MOFs. Moreover, the average bond length of the nearest Mn-O bonds in MCCF/NiMn-MOFs is about 2.12 Å, clearly longer than that of Ni-O bonds (2.05 Å), indicating a relatively weaker interaction between Mn sites and the nearest O atoms.<sup>[40]</sup>

In addition to XAFS analyses, X-ray photoelectron spectroscopy (XPS) characterization was also conducted to clarify the intrinsic electronic structure of Ni and Mn nodes in MCCF/NiMn-MOFs (Figure 3c,d; Figure S11, SI). As shown in Figure 3c, the two dominant peaks located at 855.8 and 857.4 eV can be well assigned to the 2p<sub>3/2</sub> of Ni<sup>2+</sup> and Ni<sup>3+</sup> species, respectively.<sup>[32,41]</sup> Similarly, the deconvolution results of Mn 2p XPS (Figure 3d) show that there are two main peaks at 640.9 and 642.5 eV, which are ascribed to the 2p<sub>3/2</sub> of Mn<sup>3+</sup> and Mn<sup>4+</sup> species, respectively.<sup>[42,43]</sup> These XPS analyses suggest the co-existence of Ni<sup>2+/3+</sup> and Mn<sup>3+/4+</sup> species in MCCF/NiMn-MOFs. It is noted that the white-line peak of Ni *K*-edge X-ray absorption near edge structure (XANES) spectroscopy of MCCF/NiMn-MOFs becomes slightly stronger in intensity relative to MCCF/Ni-MOFs, with the incorporation of Mn nodes (Figure S12, SI), implying the reduced electron occupancy in the outermost Ni 3d orbit in MCCF/NiMn-MOFs.<sup>[44]</sup> The mixed high valence Ni<sup>2+/3+</sup> and Mn<sup>3+/4+</sup>, as well

as their octahedral configurations of  $\text{NiO}_6$  and  $\text{MnO}_6$ , are expected to enable NiMn-MOFs with high oxygen electrocatalytic performance, which can also be seen in transition-metal oxyhydroxides that possess similar metal valences and structural configurations.<sup>[40,45]</sup>

To evaluate the electrocatalytic performance of MCCF/NiMn-MOFs, both ORR and OER measurements were conducted in alkaline solutions by using a standard three-electrode working system, with MCCF/Ni-MOFs (Figure S13, S14, SI), physical mixture of NiMn-MOF particles and MCCF (NiMn-MOFs+MCCF, Figure S15, S16, SI), and benchmark Pt/C (20 wt%) or  $\text{RuO}_2$  as references. The linear sweep voltammetry (LSV) plots (**Figure 4a**) and cyclic voltammetry (CV) curves (Figure S17, SI) show that MCCF/NiMn-MOFs manifest excellent ORR activity with an onset potential ( $E_0$ ) of 0.85 V vs. RHE and a large limiting current density ( $J_L$ ) of  $\sim 5.6 \text{ mA cm}^{-2}$ , comparable with that of Pt/C (0.91 V,  $\sim 5.4 \text{ mA cm}^{-2}$ ) and superior to those of MCCF/Ni-MOFs (0.77 V,  $\sim 3.5 \text{ mA cm}^{-2}$ ) and NiMn-MOFs+MCCF (0.81 V,  $\sim 4.5 \text{ mA cm}^{-2}$ ). Furthermore, the ORR half-wave potential ( $E_{1/2}$ ) of MCCF/NiMn-MOFs is about 0.73 V vs. RHE, significantly outperforming those of MCCF/Ni-MOFs (0.60 V vs. RHE) and NiMn-MOFs+MCCF (0.64 V vs. RHE). Moreover, MCCF/NiMn-MOFs manifest a good turnover frequency (TOF; Figure S18a, SI) with a typical value of  $0.17 \text{ s}^{-1}$  at 0.5 V vs. RHE, and a low  $\text{H}_2\text{O}_2$  yield percentage of less than 5% (Figure S19, SI) during the ORR process. Based on the LSV plots (Figure 4b) and Koutechy-Levich (K-L) plots (Figure S20, SI), the calculated electron transfer number of MCCF/NiMn-MOFs is estimated to be about 3.86, corresponding to an efficient  $4e^-$  ORR pathway. It is noteworthy that both the  $E_0$  and  $J_L$  of NiMn-MOFs+MCCF obviously outperform that of MCCF/Ni-MOFs, indicating a positive role of the bimetallic synergy of Ni and Mn nodes in ORR performance. Moreover, the chronoamperometric curves in Figure 4c and Figure S21a (SI) show much better stability and methanol tolerance of MCCF/NiMn-MOFs than that of commercial Pt/C (20 wt%). Retentions of about 95% and 92% of the initial current are achieved for MCCF/NiMn-MOFs after 10-hour and 30-hour ORR operations,

respectively, even in the presence of methanol, while a sudden loss of about 30% of the initial activity is observed for Pt/C upon the addition of methanol.

In addition to high ORR activity, MCCF/NiMn-MOFs also exhibit good OER performance. As shown in Figure 4d, MCCF/NiMn-MOFs initially drive OER at a low  $E_0$  of 1.43 V vs. RHE and then deliver  $10 \text{ mA cm}^{-2}$  at a small overpotential ( $\eta$ ) of 280 mV, much superior to MCCF/Ni-MOFs (430 mV), NiMn-MOFs+MCCF (320 mV), and  $\text{RuO}_2$  (410 mV). Furthermore, a smaller Tafel slope of  $86 \text{ mV dec}^{-1}$  is obtained for MCCF/NiMn-MOFs (Figure 4e) relative to MCCF/Ni-MOFs ( $112 \text{ mV dec}^{-1}$ ) and NiMn-MOFs+MCCF ( $93 \text{ mV dec}^{-1}$ ), indicating faster OER kinetics. MCCF/NiMn-MOFs also display a relatively high TOF with a typical value of  $0.32 \text{ s}^{-1}$  at  $\eta = 300 \text{ mV}$  (Figure S18b, SI), and a superior faradaic efficiency of more than 91% (Figure S22, SI) during the OER process. Moreover, the surface double-layer capacitance ( $C_{dl}$ ), which is closely proportional to the electrochemically active surface area (ECSA) of electrocatalysts,<sup>[21]</sup> is estimated to be  $4.37 \text{ mF cm}^{-2}$  for MCCF/NiMn-MOFs (Figure S23, SI), much larger than that of MCCF/Ni-MOFs ( $2.14 \text{ mF cm}^{-2}$ ) and NiMn-MOFs+MCCF ( $3.62 \text{ mF cm}^{-2}$ ). This result suggests more active sites are exposed in MCCF/NiMn-MOFs. The electrochemical impedance spectroscopy (EIS) results (Figure S24, SI) show the smallest semi-circle for MCCF/NiMn-MOFs relative to MCCF/Ni-MOFs and NiMn-MOFs+MCCF, indicating a great improvement in charge transfer for MCCF/NiMn-MOFs. Remarkably, nearly 100% and about 96% of the initial activity of MCCF/NiMn-MOFs are maintained after 10-hour and 30-hour OER tests, respectively, in contrast to a total loss of about 33% of the initial activity for the benchmark  $\text{RuO}_2$  (Figure 4f; Figure S21b, SI). Additionally, the sheet-like morphology and monoclinic structure of NiMn-MOFs are well preserved after the long-term ORR and OER tests (Figures S25-28, SI), confirming the excellent electrochemical stability of MCCF/NiMn-MOFs towards both ORR and OER in alkaline solutions. In view of the  $E_0$  and/or  $\eta_{10}$  as well as the large  $J_L$ , MCCF/NiMn-MOFs can be regarded as one of the most promising MOF-based oxygen



electrocatalysts reported which generally deliver  $E_0$  values of 0.8-0.9 V vs. RHE for ORR and  $\eta_{10}$  values of 240-330 mV for OER (Table S2 and S3, SI).<sup>[14,28,34,38]</sup>

Theoretical investigations based on DFT calculations were performed to shed light on the origin of oxygen electrocatalytic activity for MCCF/NiMn-MOFs. The density of states (DOS) for Ni-MOFs and NiMn-MOFs (**Figure 5a**; Figures S29-31, SI) is first calculated for comparison. There is no electron density around the Fermi level of Ni-MOFs, exhibiting a semiconductor-like electronic structure.<sup>[46]</sup> In sharp contrast, obvious electron density around the Fermi level of NiMn-MOFs is observed, suggesting the presence of free electrons after the incorporation of Mn nodes.<sup>[47]</sup> Furthermore, the calculated partial density of states (PDOS) in Figure 5b,c depicts that the enhanced DOS around the Fermi level of NiMn-MOFs is mainly derived from the hybrid of Ni 3d and O 2p orbitals, rather than that of Mn and O, implying a stronger interaction between Ni and the nearest O atoms. Specifically, the Fermi level of NiMn-MOFs comes across the 3d orbital band of Ni, enabling Ni sites as both electron donors and acceptors towards efficient electrochemical redox reactions.<sup>[40,47]</sup> In comparison, the dominant 3d orbital band of Mn is far away from the Fermi level and mainly locates at a relatively higher energy position, suggesting Mn sites as favorable electron acceptors.

The theoretical adsorption energies of ORR and OER reactants, such as  $O_2$  and  $OH^-$  species, on the surface of NiMn-MOFs are calculated to identify the active sites of MCCF/NiMn-MOFs for oxygen electrocatalysis. As shown in Figure 5d, it can be found that the adsorption energies of  $O_2$  and  $OH^-$  species on Ni sites of NiMn-MOFs are about -1.89 and -2.46 eV respectively, much lower than that on adjacent Mn sites (-1.16 and -2.01 eV). These results indicate the Ni sites serve as the potentially active metal centers for both ORR and OER. During ORR and OER processes in alkaline solutions, the adsorption of water molecules ( $H_2O$ ) on the surface of catalysts plays an important role in the corresponding proton-coupled electron transfer kinetics, due to the effective proton donors of adsorbed water molecules.<sup>[2,12]</sup> Interestingly, the adsorption energy of  $H_2O$  over Mn sites (-0.78 eV) is much lower than that over Ni sites (-0.52 eV), meaning Mn sites serve as more energetic sites for

H<sub>2</sub>O adsorption (Figure 5e). This adsorbed H<sub>2</sub>O over Mn sites may thermodynamically prefer to couple with the reactants of O<sub>2</sub> or OH<sup>-</sup> species that are adsorbed over adjacent Ni sites, contributing to a great promotion in the formation of key intermediates during the ORR and OER processes.<sup>[3]</sup> An increase of Ni<sup>3+</sup>/Ni<sup>2+</sup> ratio along with a slightly decreased Mn<sup>4+</sup>/Mn<sup>3+</sup> ratio is observed for MCCF/NiMn-MOFs after OER tests (Figure 3c,d; Figure S28, SI), which further suggests that Ni acts as the real active sites and Mn serves as the synergetic sites for oxygen electrocatalysis. In general, the generation of key \*O or \*OOH intermediates over active metal sites of MOF-based catalysts has been regarded as the rate-determining step (RDS) for ORR or OER, owing to the high energy requirement for the dissociation or formation of O-O bonds.<sup>[3,48]</sup> As shown in Figure 5f, the formation energy barriers of key \*O and \*OOH intermediates over Ni sites in NiMn-MOFs are 1.17 and 0.89 eV, respectively, which are much lower than that in Ni-MOFs (2.43 and 2.04 eV), indicating more efficient kinetics in NiMn-MOFs towards both ORR and OER. Accordingly, with the synergetic effect between neighboring Ni and Mn nodes, the proton-coupled electron transfer kinetics could be greatly accelerated during ORR and OER processes, resulting in high oxygen electrocatalytic activity for NiMn-MOFs.

The high electrocatalytic performance of MCCF/NiMn-MOFs is due to not only the synergetic interactions between Ni and Mn nodes but also the well-designed architecture. Specially, the sheet-like morphology of NiMn-MOFs fully exposes the highly active bimetal centers on the surface, as verified by the ECSA characterization (Figure S23, S24a, SI), which significantly increases the amount of active sites for ORR and OER. In addition, the tight connection between the highly conductive MCCF support and NiMn-MOF nanosheets guarantees the efficient charge transfer and robust stability, in line with the electrochemical results of EIS spectra (Figure S24b, SI) and i-t curves (Figure 4c,f; Figure S21, SI). Moreover, the multi-level pore structure of macropores in the interwoven MCCF support and mesopores in each MCCF promotes the easy permeation of reactive species in solution as well as the fast mass transport of oxygen, thus contributing to accelerated ORR

and OER kinetics. Overall, by taking advantages of the synergetic interactions between  $\text{Ni}^{2+/3+}$  and  $\text{Mn}^{3+/4+}$  nodes and the rational hierarchical architecture, the MCCF/NiMn-MOFs are demonstrated as a promising bifunctional electrocatalyst with high activity and stability towards both ORR and OER.

In summary, NiMn-based bimetal-organic framework (NiMn-MOF) nanosheets supported on multi-channel carbon fiber (MCCF) are rationally designed and synthesized as a promising noble-metal-free bifunctional oxygen electrocatalyst via a facile hydrothermal and subsequent ligand exchange strategy. Combining the atomic-level synchrotron radiation characterizations and the in-depth theoretical calculations, the nature of electrocatalytic active sites and the origin of electrochemical activity are revealed in detail for MCCF/NiMn-MOFs, where the strong synergetic effect of neighboring Ni and Mn nodes enables active  $\text{NiO}_6$  centers of NiMn-MOFs with fast ORR and OER kinetics. This work may provide new insights into the design of cost-effective MOF-based bifunctional oxygen electrocatalysts towards energy-related applications.

## Acknowledgments

X.W.L. acknowledges the funding support from the Ministry of Education of Singapore through the Academic Research Fund (AcRF) Tier-1 funding (RG116/18), and the National Research Foundation (NRF) of Singapore via the NRF Investigatorship (NRF-NRFI2016-04). The authors thank Dr. Shibo Xi and the X-ray absorption fine structure for catalysis (XAFCA) beamline of the Singapore Synchrotron Light Source (SSLS) for supporting the XAFS measurements.

## References

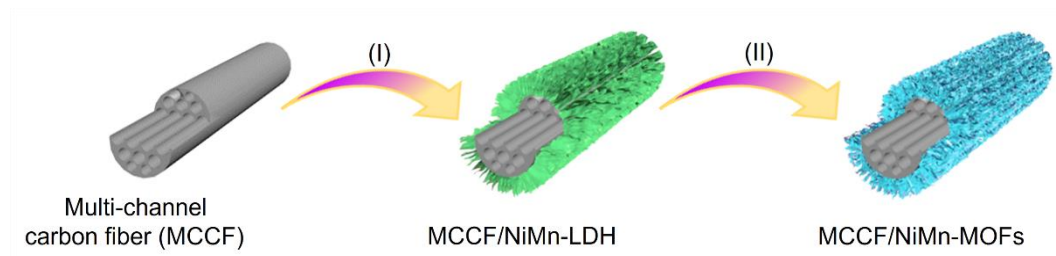
- [1] V. R. Stamenkovic, D. Strmcnik, P. P. Lopes, N. M. Markovic, *Nat. Mater.* **2017**, *16*, 57.
- [2] N. T. Suen, S. F. Hung, Q. Quan, N. Zhang, Y. J. Xu, H. M. Chen, *Chem. Soc. Rev.* **2017**, *46*, 337.
- [3] Z. W. Seh, J. Kibsgaard, C. F. Dickens, I. B. Chorkendorff, J. K. Nørskov, T. F. Jaramillo, *Science* **2017**, *355*, eaad4998.
- [4] J. W. Nai, X. W. Lou, *Adv. Mater.* **2019**, *31*, 1706825.
- [5] X. F. Lu, Y. Chen, S. B. Wang, S. Y. Gao, X. W. Lou, *Adv. Mater.* **2019**, *31*, 1902339.

- [6] Z. P. Wu, X. F. Lu, S. Q. Zang, X. W. Lou, *Adv. Funct. Mater.* **2020**, *30*, 1910274.
- [7] X. F. Lu, B. Y. Xia, S. Q. Zang, X. W. Lou, *Angew. Chem. Int. Ed.* **2020**, *59*, 4634.
- [8] M. H. Shao, Q. W. Chang, J. P. Dodelet, R. Chenitz, *Chem. Rev.* **2016**, *116*, 3594.
- [9] L. Z. Bu, N. Zhang, S. J. Guo, X. Zhang, J. Li, J. L. Yao, T. Wu, G. Lu, J. Y. Ma, D. Su, X. Q. Huang, *Science* **2016**, *354*, 1410.
- [10] H. Zhang, P. An, W. Zhou, B. Y. Guan, P. Zhang, J. Dong, X. W. Lou, *Sci. Adv.* **2018**, *4*, eaao6657.
- [11] A. S. Kelsey, R. R. Reshma, R. W. Xiao, T. H. Wesley, M. R. Christopher, S. H. Yang, *Chem* **2017**, *2*, 668.
- [12] Z. Huang, J. Wang, Y. Peng, C. Jung, A. Fisher, X. Wang, *Adv. Energy Mater.* **2017**, *7*, 1700544.
- [13] S. Lee, E. A. Kapustin, O. M. Yaghi, *Science* **2016**, *353*, 808.
- [14] W. Cheng, X. Zhao, H. Su, F. Tang, W. Che, H. Zhang, Q. Liu, *Nat. Energy* **2019**, *4*, 115.
- [15] D. Zhao, Z. Zhuang, X. Cao, C. Zhang, Q. Peng, C. Chen, Y. Li, *Chem. Soc. Rev.* **2020**, *49*, 2215.
- [16] B. Y. Xia, Y. Yan, N. Li, H. B. Wu, X. W. Lou, X. Wang, *Nat. Energy* **2016**, *1*, 15006.
- [17] M. Lions, J. B. Tommasino, R. Chattot, B. Abeykoon, N. Guillou, T. Devic, A. Demessence, L. Cardenas, F. Maillard, A. Fateeva, *Chem. Commun.* **2017**, *53*, 6496.
- [18] X. F. Lu, P. Q. Liao, J. W. Wang, J. X. Wu, X. W. Chen, C. T. He, J. P. Zhang, G. R. Li, X. M. Chen, *J. Am. Chem. Soc.* **2016**, *138*, 8336.
- [19] T. D. Bennett, A. K. Cheetham, A. H. Fuchs, F. X. Coudert, *Nat. Chem.* **2017**, *9*, 11.
- [20] H. F. Wang, L. Chen, H. Pang, S. Kaskel, Q. Xu, *Chem. Soc. Rev.* **2020**, *49*, 1414.
- [21] D. Sheberla, J. C. Bachman, J. S. Elias, C. J. Sun, S. H. Yang, M. Dinca, *Nat. Mater.* **2017**, *16*, 220.
- [22] D. W. Feng, T. Lei, M. R. Lukatskaya, J. Park, Z. H. Huang, M. Lee, L. Shaw, S. C. Chen, A. A. Yakovenko, A. Kulkarni, J. P. Xiao, K. Fredrickson, J. B. Tok, X. D. Zou, Y. Cui, Z. N. Bao, *Nat. Energy* **2018**, *3*, 30.
- [23] S. Yuan, L. Feng, K. Wang, J. Pang, M. Bosch, C. Lollar, Y. Sun, J. Qin, X. Yang, P. Zhang, Q. Wang, L. Zou, Y. Zhang, L. Zhang, Y. Fang, J. Li, H. C. Zhou, *Adv. Mater.* **2018**, *30*, 1704303.
- [24] L. Chen, Z. Xu, W. Han, Q. Zhang, Z. Bai, Z. Chen, G. Li, X. Wang, *ACS Appl. Nano Mater.* **2020**, *3*, 1354.
- [25] P. He, X. Y. Yu, X. W. Lou, *Angew. Chem. Int. Ed.* **2017**, *56*, 3897.
- [26] P. Zhang, X. F. Lu, J. W. Nai, S. Q. Zang, X. W. Lou, *Adv. Sci.* **2019**, *6*, 1900576.
- [27] S. B. Liu, X. F. Lu, J. Xiao, X. Wang, X. W. Lou, *Angew. Chem. Int. Ed.* **2019**, *58*, 13828.
- [28] Y. Wang, Y. Liu, H. Wang, W. Liu, Y. Li, J. Zhang, H. Hou, J. Yang, *ACS Appl. Energy Mater.* **2019**, *2*, 2063.
- [29] W. R. Cheng, H. Zhang, X. Zhao, H. Su, F. M. Tang, J. Tian, Q. H. Liu, *J. Mater. Chem. A* **2018**,

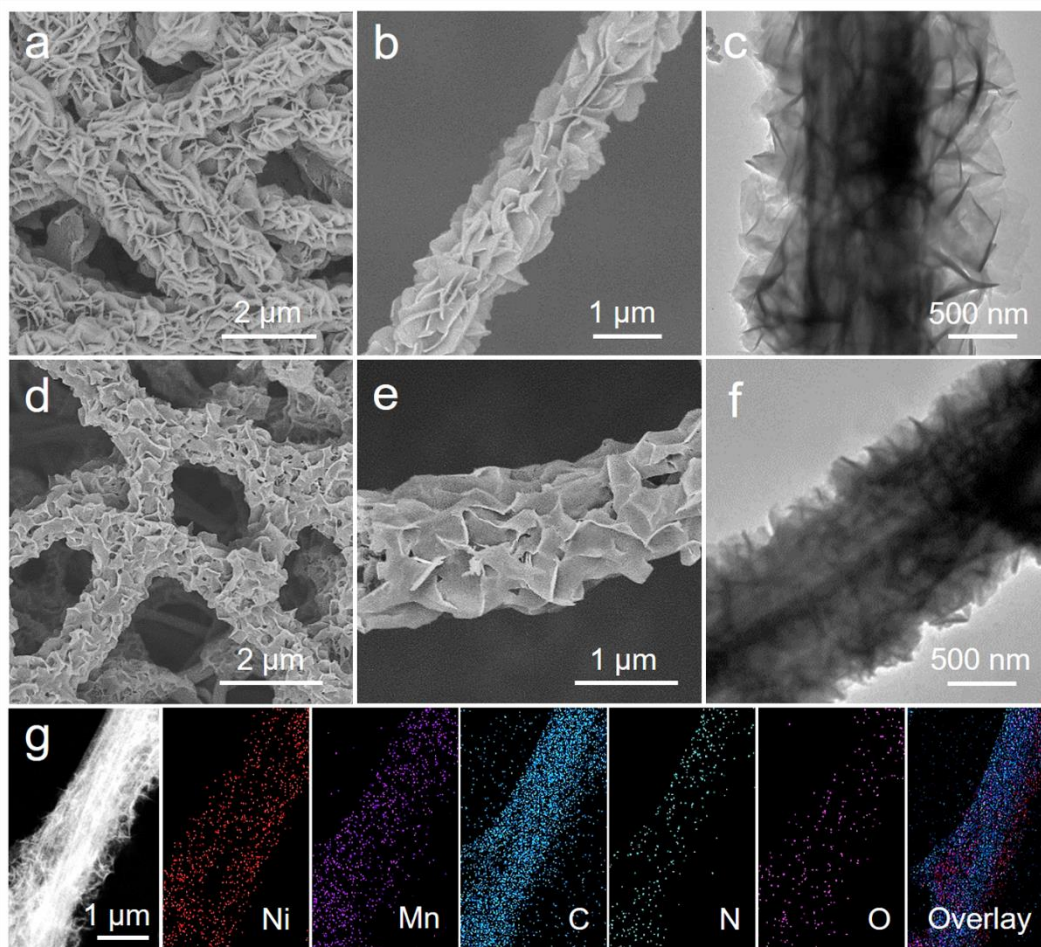
6, 9420.

- [30] K. Achelhi, S. Masse, G. Lautent, A. Saoiabi, A. Laghzizil, T. Coradin, *Dolton Trans.* **2010**, *39*, 10644.
- [31] Z. Chen, J. Yang, W. Cheng, J. Huang, D. Yang, Y. Xue, X. Wu, *Transit. Met. Chem.* **2020**, *45*, 121.
- [32] B. Wang, J. Shang, C. Guo, J. Zhang, F. Zhu, A. Han, J. Liu, *Small* **2019**, *15*, 1804761.
- [33] J. Chen, X. Wang, J. Wang, P. S. Lee, *Adv. Energy Mater.* **2016**, *6*, 1501745.
- [34] J. J. Duan, S. Chen, C. Zhao, *Nat. Commun.* **2017**, *8*, 15341.
- [35] T. Gholam, L. R. Zheng, J. O. Wang, H. J. Qian, R. Wu, H. Q. Wang, *Nanoscale Res. Lett.* **2019**, *14*, 137.
- [36] Y. Amit, Y. Y. Li, A. I. Frenkel, U. Banin, *ACS Nano* **2015**, *9*, 10790.
- [37] H. L. Duan, P. Guo, C. Wang, H. Tan, W. Hu, W. S. Yan, C. Ma, L. Cai, L. Song, W. H. Zhang, Z. H. Sun, L. J. Wang, W. B. Zhao, Y. W. Yin, X. G. Li, S. Q. Wei, *Nat. Commun.* **2019**, *10*, 1584.
- [38] S. L. Zhao, Y. Wang, J. C. Dong, C. T. He, H. J. Yin, P. F. An, K. Zhao, X. F. Zhang, C. Gao, L. J. Zhang, J. W. Lv, J. X. Wang, J. Q. Zhang, A. M. Khattak, N. A. Khan, Z. X. Wei, J. Zhang, S. Q. Liu, H. J. Zhao, Z. Y. Tang, *Nat. Energy* **2016**, *1*, 16184.
- [39] Q. He, D. Tian, H. Jiang, D. Cao, S. Wei, D. Liu, P. Song, Y. Lin, L. Song, *Adv. Mater.* **2020**, *32*, 1906972.
- [40] M. Gorlin, P. Chernev, J. Ferreira de Araujo, T. Reier, S. Dresch, B. Paul, R. Krahner, H. Dau, P. Strasser, *J. Am. Chem. Soc.* **2016**, *138*, 5603.
- [41] H. M. Sun, Y. X. Ye, Z. F. Tian, S. L. Wu, J. Liu, C. H. Liang, *RSC Adv.* **2017**, *7*, 49010.
- [42] X. Xu, W. Shi, W. Liu, S. Ye, R. Yin, L. Zhang, L. Xu, M. Chen, M. Zhong, X. Cao, *J. Mater. Chem. A* **2018**, *6*, 24086.
- [43] F. O. Ochai-Ejeh, M. J. Madito, D. Y. Momodu, A. A. Khaleed, O. Olaniyan, N. Manyala, *Electrochim. Acta* **2017**, *252*, 41.
- [44] M. Wang, L. Árnadóttir, Z. J. Xu, Z. Feng, *Nanomicro Lett.* **2019**, *11*, 47.
- [45] A. Bergmann, T. E. Jones, E. M. Moreno, D. Teschner, P. Chernev, M. Gliech, T. Reier, H. Dau, P. Strasser, *Nat. Catal.* **2018**, *1*, 711.
- [46] Y. Li, Y. Fu, B. Ni, K. Ding, W. Chen, K. Wu, X. Huang, Y. Zhang, *AIP Adv.* **2018**, *8*, 035012.
- [47] J. R. Petrie, V. R. Cooper, J. W. Freeland, T. L. Meyer, Z. Y. Zhang, D. A. Lutterman, H. N. Lee, *J. Am. Chem. Soc.* **2016**, *138*, 2488.
- [48] M. Bajdich, M. Garcia-Mota, A. Vojvodic, J. K. Nørskov, A. T. Bell, *J. Am. Chem. Soc.* **2013**, *135*, 13521.

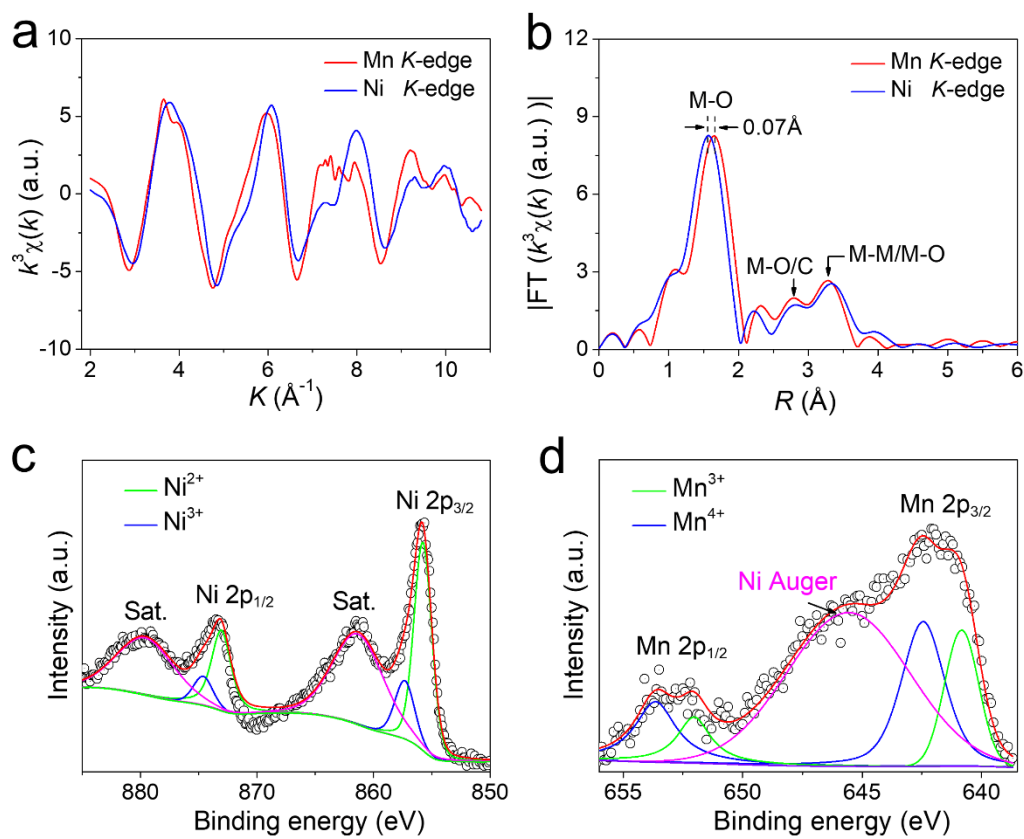
## Figures and Captions



**Figure 1.** Schematic illustration of the synthetic process for the MCCF/NiMn-MOFs. (I) hydrothermal reaction to form MCCF/NiMn-LDH, (II) conversion to MCCF/NiMn-MOFs through a subsequent ligand exchange reaction.

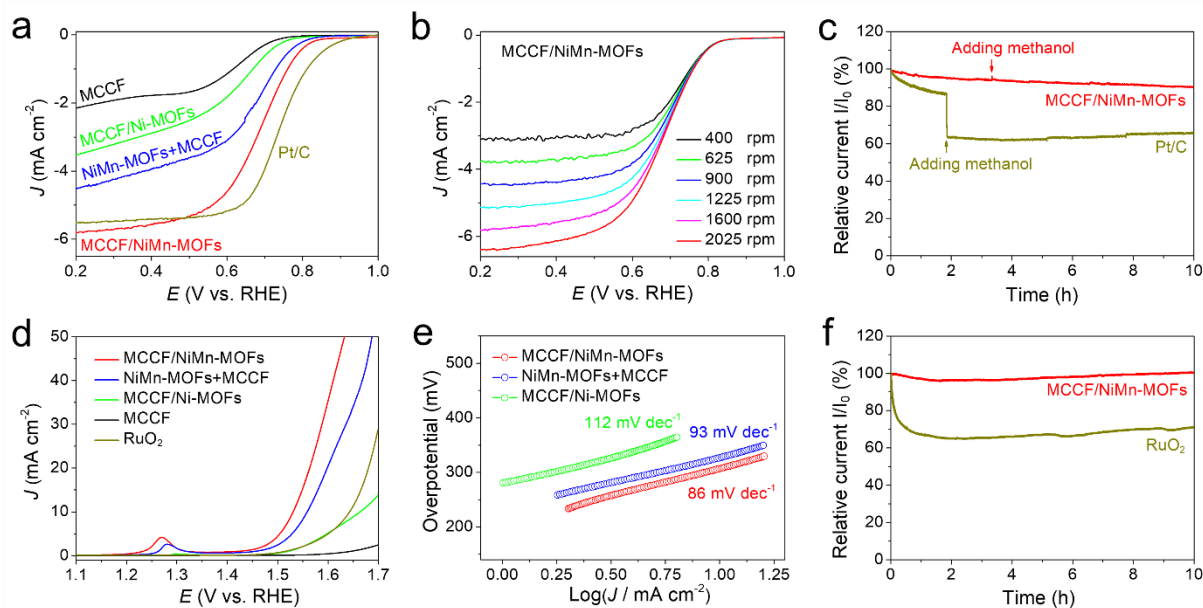


**Figure 2.** (a, b) FESEM and (c) TEM images of MCCF/NiMn-LDH; (d, e) FESEM, (f) TEM, and (g) HAADF-STEM image and corresponding elemental mapping images of MCCF/NiMn-MOFs.

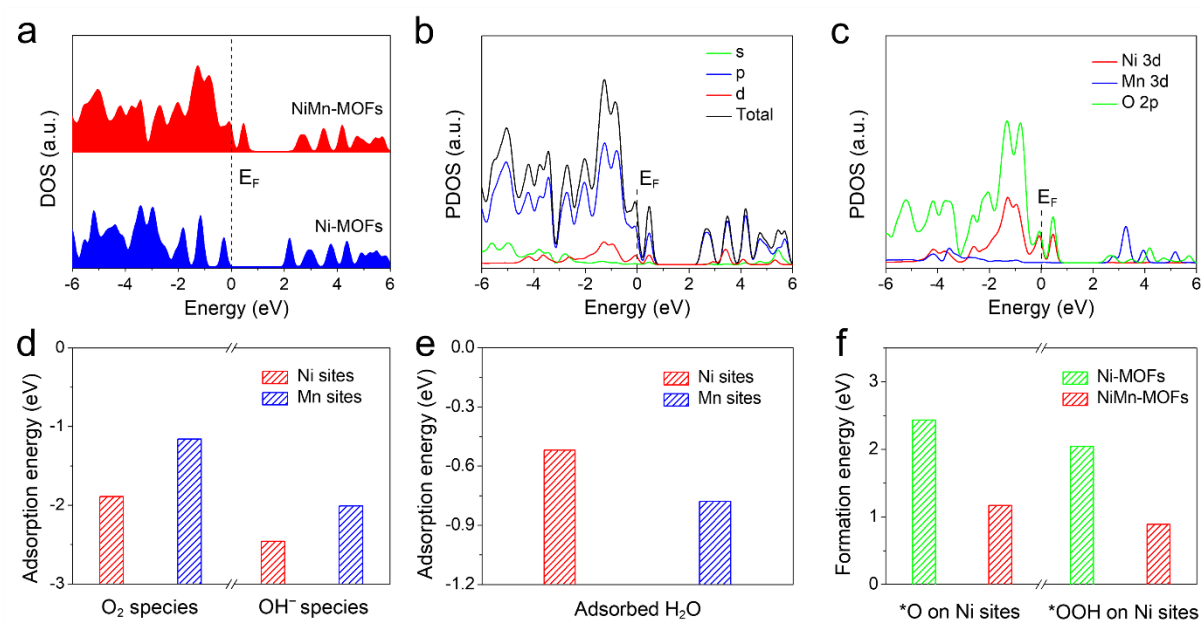


**Figure 3.** (a)  $k^3\chi(k)$  oscillation curves, (b) Fourier transform curves of the Ni and Mn K-edge EXAFS spectra, (c) Ni 2p XPS spectrum, and (d) Mn 2p XPS spectrum of MCCF/NiMn-MOFs.



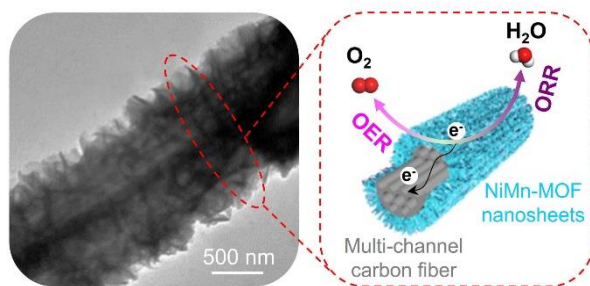


**Figure 4.** (a-c) ORR performance in 0.1 M KOH solution: LSV plots at 1600 revolutions per minute (rpm) (a) and MCCF/NiMn-MOFs under various rotating speeds (b); chronoamperometric (i-t) curves with the addition of methanol for Pt/C and MCCF/NiMn-MOFs (c). (d-f) OER performance in 1.0 M KOH solution: LSV plots (d), the corresponding Tafel slopes for MCCF/Ni-MOFs, NiMn-MOFs+MCCF and MCCF/NiMn-MOFs (e), and i-t curves for RuO<sub>2</sub> and MCCF/NiMn-MOFs (f).



**Figure 5.** (a) Calculated density of states (DOS) for Ni-MOFs and NiMn-MOFs, (b, c) calculated partial density of states (PDOS) for NiMn-MOFs. Adsorption energy of (d)  $O_2$  and  $OH^-$  as well as (e)  $H_2O$  reactants on Ni and Mn sites in NiMn-MOFs. (f) Formation energy of  $*O$  and  $*OOH$  intermediates for Ni-MOFs and NiMn-MOFs.

for Table of Content Entry



**NiMn-based bimetal-organic framework nanosheets** are successfully grown on multi-channel carbon fibers (MCCF/NiMn-MOFs) as a promising bifunctional oxygen electrocatalyst. The strong synergetic effect of bimetallic nodes as well as the well-designed hierarchical architecture is unraveled to enable MCCF/NiMn-MOFs with fast kinetics and robust stability towards efficient oxygen electrocatalysis.